

# Inversion-symmetry engineering in layered oxide thin films

J. Nordlander,<sup>1,\*</sup> M. D. Rossell,<sup>2</sup> M. Campanini,<sup>2</sup> M. Fiebig,<sup>1</sup> and M. Trassin<sup>1,†</sup>

<sup>1</sup>*Department of Materials, ETH Zurich, CH-8093 Zurich, Switzerland*

<sup>2</sup>*Electron Microscopy Center, Empa, CH-8600 Dübendorf, Switzerland*

## Abstract

Inversion symmetry breaking is a ubiquitous concept in condensed-matter science. On the one hand, it is a prerequisite for technologically relevant effects such as piezoelectricity, photovoltaic and nonlinear optical properties and spin-transport phenomena. On the other hand, it determines abstract properties such as the electronic topology in quantum materials. Therefore, the creation of materials where inversion symmetry can be turned on or off by design may be the ultimate route towards controlling parity-related phenomena and functionalities. Here, we engineer the symmetry of ultrathin epitaxial oxide films by sub-unit-cell growth control. We reversibly activate and deactivate inversion symmetry in the layered hexagonal manganites, h-RMnO<sub>3</sub> with R = Y, Er, Tb. We set the desired state by tracking the growth *in situ* via optical second-harmonic generation. While an odd number of half-unit-cell layers exhibits a breaking of inversion symmetry through its arrangement of MnO<sub>5</sub> bipyramids, an even number of such half-unit-cell layers is centrosymmetric. Our symmetry engineering works independent of the choice of R and even in heterostructures mixing constituents with different R in a two-dimensional growth mode. Symmetry engineering on the sub-unit-cell level thus suggests a new platform for the controlled activation and deactivation of symmetry-governed functionalities in oxide-electronic epitaxial thin films.

---

\* johanna.nordlander@mat.ethz.ch

† morgan.trassin@mat.ethz.ch

## INTRODUCTION

According to the fundamental Neumann principle, the symmetry of a material is reflected in its physical properties. Hence, whenever a symmetry is broken, new functionalities arise<sup>1</sup>. A special case is inversion symmetry. It assigns a parity of +1 or -1 to the transformation property of physical processes under the inversion operation. Symmetries of this type play a fundamental role in conservation laws and the associated physical phenomena. For example, in the field of quantum materials, the conservation or breaking of inversion symmetry distinguishes Dirac from Weyl semimetals<sup>2</sup>. Also many technologically relevant phenomena, like piezoelectricity, photovoltaics and spin-transport effects, depend on a broken inversion symmetry<sup>3-5</sup>.

The symmetry of a material may be broken spontaneously. For example, in ferroelectrics, spatial inversion symmetry is lost by the onset of spontaneous polarization, giving rise to the very phenomenon which established their technological relevance: piezoelectricity. However, relying on the occurrence of a spontaneous symmetry breaking for enabling a desired functionality in a material lacks control. It would rather be preferable to set the symmetry of a material on demand. Recent progress in materials engineering now allows to achieve inversion-symmetry breaking by design. For example, by combining dissimilar materials into heterostructures, thus disrupting the long-range crystalline order, novel states can be created at the interface between the constituents<sup>6</sup>, resulting in phenomena like two-dimensional (2D) superconductivity<sup>7</sup> or emergent magnetic and polar properties<sup>8-10</sup>. In exfoliated 2D materials, the breaking of inversion symmetry on the atomic-monolayer level can lead to a unique electronic band structure<sup>11</sup>, valley-selectivity<sup>12</sup>, electronic edge-states and nonlinear optical response<sup>13-15</sup>.

All this emphasizes the fundamental importance of inversion symmetry – or rather its absence – for functional properties in materials and it highlights the need for deterministic control of inversion-symmetry breaking as a key aspect in state-of-the-art materials engineering. In the vast family of functional oxides, the naturally layered compounds stand out as prime candidates for this purpose. In these materials, the unit cell itself is layered, and these layers exhibit a different symmetry than the unit cell in its entity. The sub-unit-cell building blocks may therefore locally exhibit properties that are not permitted for the material as a whole. This aspect has been little explored, however.

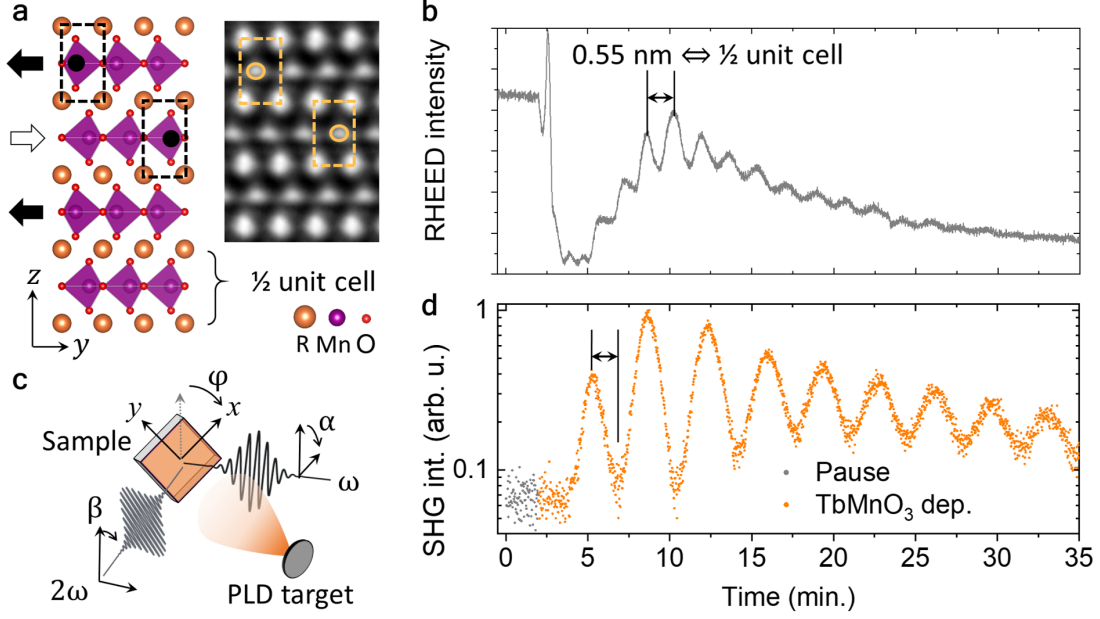


FIG. 1. **Probing inversion symmetry during h-RMnO<sub>3</sub> growth.** **a** Prototype crystal structure of the h-RMnO<sub>3</sub> family and a corresponding STEM image of a h-YMnO<sub>3</sub> film. The noncentrosymmetric structure of each half-unit-cell layer and their alternating orientation are highlighted by dashed boxes. **b** RHEED intensity oscillations indicate a layer-by-layer growth mode with each layer representing half a unit cell. **c** Experimental ISHG setup. The sample is probed in a reflection geometry in the PLD growth chamber during deposition and (not shown) with simultaneous RHEED monitoring. The angle of polarization of the fundamental ( $\omega$ ) and the SHG ( $2\omega$ ) light are given by  $\alpha$  and  $\beta$ , respectively. The azimuthal angle  $\varphi$  denotes the orientation of the  $x$  axis of the sample with respect to the vertical axis of the laboratory. **d** ISHG intensity during deposition of 10 nm (9 unit cells) of h-TbMnO<sub>3</sub> detected at  $(\alpha, \beta) = (90^\circ, 120^\circ)$ . Calibration by means of the RHEED data reveals a periodicity of the ISHG intensity oscillations of 1 unit cell.

Here, we demonstrate symmetry engineering in ultrathin layered oxides, moving repeatedly between a centrosymmetric and a noncentrosymmetric state of the material, by exerting growth control on the sub-unit-cell level. As our model system, we choose the hexagonal manganites, h-RMnO<sub>3</sub> ( $R = Y, Er, Tb$ ), because of their naturally layered structure. We deposit dielectric h-RMnO<sub>3</sub> in a layer-by-layer fashion, where each layer is only half a unit cell in height. Using in-situ optical second harmonic generation (ISHG), we track and set the symmetry of the films during deposition<sup>16,17</sup>. While an even number of half-unit-cell layers retain the inversion symmetry of the parent material, an odd number of these layers

break it because of the locally noncentrosymmetric  $\text{MnO}_5$  sublattice within each half-unit-cell block. The symmetry-sensitive ISHG response follows this alternation in real time and allows us to set the symmetry state of the thin film system on demand, here within a thickness range of less than 6 Å. By expanding from h-TbMnO<sub>3</sub> to other h-RMnO<sub>3</sub> compounds and (R'MnO<sub>3</sub>)/(R''MnO<sub>3</sub>) superlattices, we further demonstrate the extraordinary precision of this symmetry control as well as its independence of choice of R. With our work, we thus establish layered oxides as a class of materials for exerting inversion-symmetry control and its functionalization in ultrathin epitaxial films.

## RESULTS

The epitaxial h-RMnO<sub>3</sub> thin films were grown by pulsed laser deposition on (111)-oriented yttria-stabilized zirconia (YSZ) substrates. Their crystal structure is shown in Fig. 1a. While the h-RMnO<sub>3</sub> compounds are usually found in a noncentrosymmetric improper ferroelectric phase, a suppression of the polar mode in the ultrathin regime places the system in the paraelectric phase during deposition<sup>18</sup>. In this phase, the unit cell is centrosymmetric and belongs to the point group  $6/mmm$ . It consists, however, of two identical noncentrosymmetric half-unit-cell layers rotated by 60° with respect to each other. The symmetry of these is  $\bar{6}m2$ , given by the structure of the  $\text{MnO}_5$  sublattice<sup>19</sup>.

For the epitaxial thin films grown by PLD, in-situ reflection high-energy electron diffraction (RHEED) intensity oscillations and post-deposition thickness analysis by x-ray reflectivity indicate a layer-by-layer growth mode where each layer corresponds to half a unit cell in height (Fig. 1b). Therefore, through precise growth control, either a centrosymmetric state (even number of half-unit-cell layers) or a noncentrosymmetric state (odd number of half-unit-cell layers) may be obtainable.

We begin by verifying the symmetry of the half-unit-cell layers in h-TbMnO<sub>3</sub> films. To access and control the thin-film properties in real time, we use ISHG during the thin-film synthesis. This technique allows probing the symmetry and related functional properties remotely and directly, as they emerge during growth<sup>16</sup>. The experimental setup is sketched in Fig. 1c. SHG is a nonlinear optical process which describes the frequency doubling of light in a material. In the electric-dipole approximation, it is described as

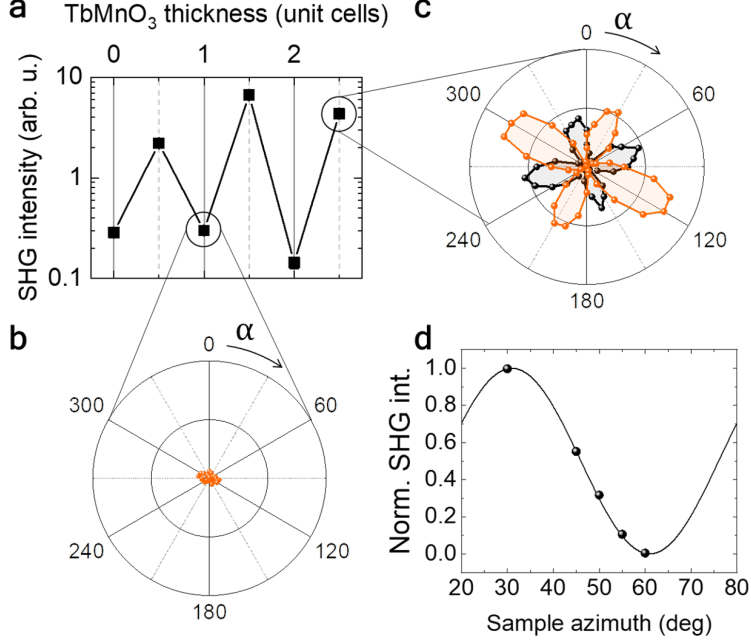


FIG. 2. **Parity control with sub-unit-cell precision in h-TbMnO<sub>3</sub> films.** **a** ISHG intensity at growth temperature for  $(\alpha, \beta) = (120^\circ, 90^\circ)$  vs. h-TbMnO<sub>3</sub> film thickness. Minima and maxima as in Fig. 1d are reproduced. **b,c** Dependence of ISHG intensity on  $\alpha$  for  $\beta = 0^\circ$  (black) and  $\beta = 90^\circ$  (orange) in the case of an **(b)** even and **(c)** odd number of half-unit-cell h-TbMnO<sub>3</sub> layers. **(b)** and **(c)** are plotted to the same scale. Because of inversion symmetry, no SHG is detected in **(b)**. The polarization dependence in **(c)** is compatible with contributions from the nonlinear susceptibility components permitted by the  $\bar{6}m2$  point symmetry of the half unit cell. We attribute the slight asymmetry among the four lobes in **(c)** to the azimuthally varying reflectivity caused by the  $90^\circ$  reflection geometry of the ISHG setup. **d** Dependence of half-unit-cell SHG intensity at  $(\alpha, \beta) = (0^\circ, 90^\circ)$  on the azimuthal orientation  $\varphi$  of the sample. The  $60^\circ$  periodicity of the data further supports the  $\bar{6}m2$  point group

$$P_i(2\omega) = \epsilon_0 \chi_{ijk}^{(2)} E_j(\omega) E_k(\omega), \quad (1)$$

where  $E_{j,k}(\omega)$  are the electric-field components of the incident fundamental beam and  $P_i(2\omega)$  denotes the resulting nonlinear polarization of the material, which then acts as source of the emitted SHG light<sup>17,20,21</sup>. The process is parameterized by the second-order susceptibility tensor  $\chi^{(2)}$ . Simultaneous monitoring of ISHG and RHEED intensities allows us to correlate the symmetry properties of the thin film with its thickness and growth mode<sup>16</sup>.

The real-time evolution of the ISHG signal while half-unit-cell layers are added one-by-one during the deposition of h-TbMnO<sub>3</sub> on YSZ is shown in Fig. 1d. A periodic modulation of the ISHG signal is observed where the intensity oscillates with a period of one unit cell. For an even number of half-unit-cell layers, no ISHG is detected. In contrast, an odd number of half-unit-cell layers results in a sizeable ISHG intensity. Strikingly, the RHEED signal oscillates twice as fast as the ISHG signal and therefore points to similar surface morphologies at the ISHG valleys and peaks. This excludes surface-morphology-related effects, such as a step density variation during the layer-by-layer growth<sup>22</sup>, as possible origin of the ISHG modulation. Instead, we attribute this modulation to the alternating symmetry of the film with the deposition of each half-unit-cell layer, as described above.

To verify this hypothesis, we analyze the polarization dependence of the ISHG signal. The ISHG response for an even and an odd number of half-unit-cell layers are shown in Figs. 2b and c, respectively. The four-lobed symmetry seen for 2.5 unit cells of h-TbMnO<sub>3</sub> in Fig. 2c is compatible with the proposed  $\bar{6}m2$  point group of a half-unit-cell layer, where the allowed  $\chi^{(2)}$  components in Eq. 1 are<sup>23</sup>:  $\chi_{yyy} = -\chi_{yxx} = -\chi_{xxy} = -\chi_{xyx}$ , with  $x$  lying parallel to the crystallographic  $a$  axis. As seen in Fig. 2d, the relation of the ISHG signal to the symmetry of the half-unit-cell lattice is further supported by the 60° periodicity of the ISHG intensity with respect to rotation of sample around its  $z$ -axis. Here, the SHG source term for the point group  $\bar{6}m2$  dictates  $P^{(2\omega)} \propto \cos(3\varphi)\chi^{(2)}$ , which leads to the SHG intensity  $I^{(2\omega)} \propto |P^{(2\omega)}|^2 \propto \sin(6\varphi)$ .

Given the polarization-independent absence of SHG for even numbers of half-unit-cell layers (Fig. 2b), we conclude, that the ISHG intensity oscillations seen in Fig. 1d are due to destructive interference of identical, yet antiphase, SHG waves from complementary half-unit-cell layers, where the antiphase relation comes from their relative 60° rotation, yielding a prefactor  $\cos(3 \cdot 60^\circ) = -1$  between the respective SHG source terms. Macroscopically, this destructive interference is in line with the vanishing  $\chi^{(2)}$  tensor for the non-polar  $6/mmm$  point group of the full unit cell. Hence, the ISHG response during growth follows the alternating breaking and restoration of inversion symmetry with the deposition of each additional half-unit-cell layer.

So far, we have restricted our discussion to h-RMnO<sub>3</sub> films with R = Tb. While our ISHG signal has proven compatible with the local symmetry of the MnO<sub>5</sub> layers, the interconnectivity between these and the R-ion layers in h-RMnO<sub>3</sub> compounds, seen for example by

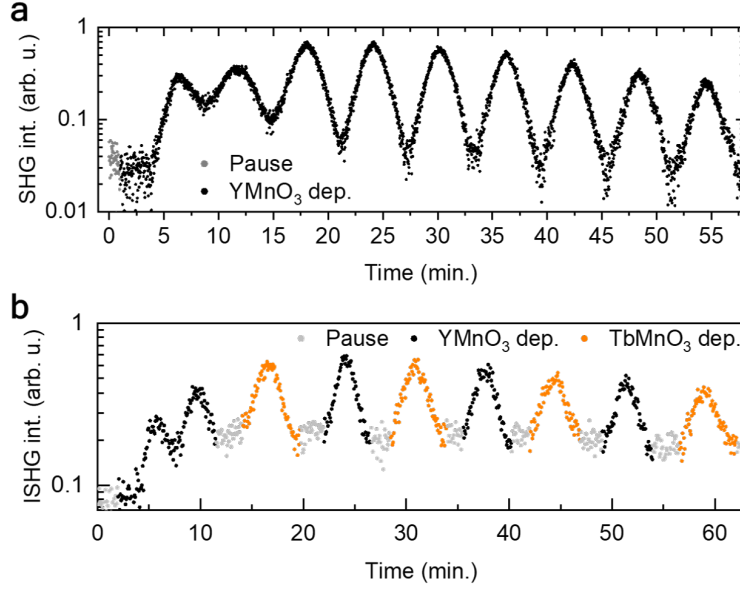


FIG. 3. **Persistence of the ISHG oscillation upon R-ion substitution.** **a** h-YMnO<sub>3</sub>. **b** (h-YMnO<sub>3</sub>)<sub>1</sub>/(h-TbMnO<sub>3</sub>)<sub>1</sub> superlattice. In both cases, the measurements correspond to 10 nm (9 unit cells) of thin-film deposition and the ISHG intensity is modulated with a period of one unit cell.

the strong correlation between MnO<sub>5</sub> tilt modes and R-ion shifts in the dominating phonon modes<sup>24</sup>, suggests a possible dependency not only on the Mn-O composition but also on the choice of R in the material.

In order to determine the influence of R, we therefore expand our investigations towards other h-RMnO<sub>3</sub> compounds. Figure 3a shows that the ISHG oscillations are also observed for the half-unit-cell by half-unit-cell-wise deposition of h-RMnO<sub>3</sub> thin films with R = Y. But even when we combine h-TbMnO<sub>3</sub> and h-YMnO<sub>3</sub> into a (h-TbMnO<sub>3</sub>)<sub>1</sub>/(h-YMnO<sub>3</sub>)<sub>1</sub> superlattice, we find that the the ISHG intensity oscillation during growth prevails (Fig. 3b). ISHG from the two compounds interferes in the same way as for the single layers and at comparable oscillation amplitudes. We can thus conclude that the ISHG signal observed here does not originate in the electronic transitions of the R-ion layer, as it behaves independently of the choice of R. Instead, it can only originate from the MnO<sub>5</sub> trigonal bipyramid layers which are uniform to all the h-RMnO<sub>3</sub> compounds.

In the comparison of the RHEED and ISHG data, it is important to note that the former technique probes the structural integrity of the sample at its surface, whereas the latter

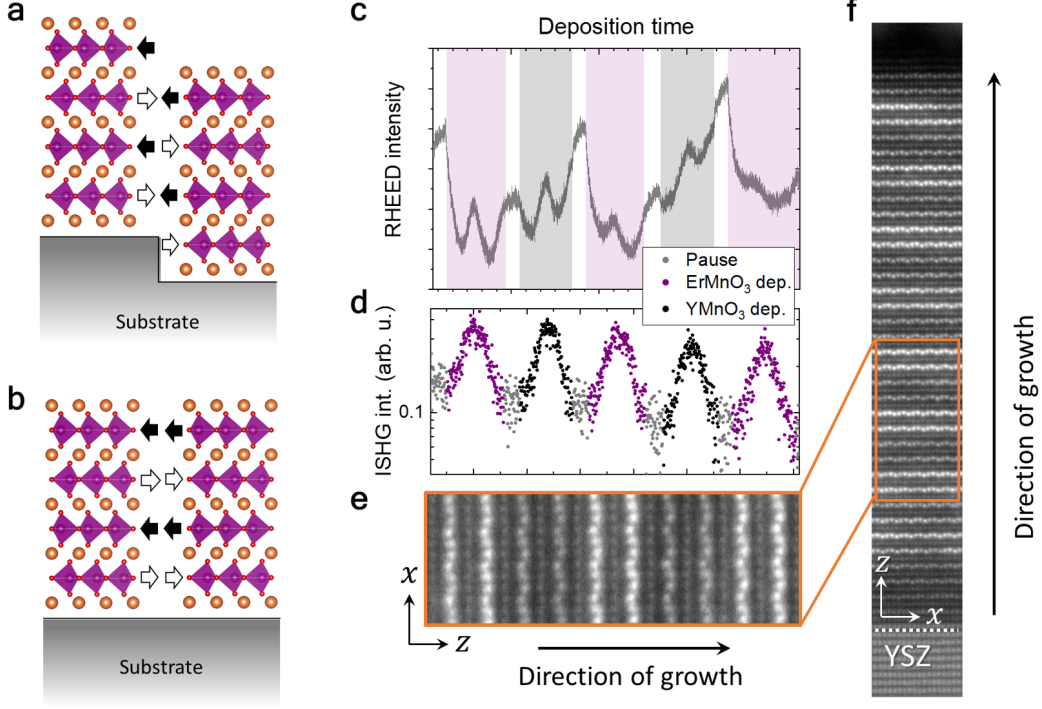


FIG. 4. **Atomic engineering using symmetry monitoring.** **a,b** Schematics showing two different surface morphologies both corresponding to a perfectly centrosymmetric structure and hence an ISHG minimum. While antiphase boundaries (**a**), for example, can result in a dephasing of RHEED and ISHG oscillations, ideal 2D growth (**b**) is characterized by concurrence of the smoothest surface (RHEED maxima) with both ISHG minima and maxima. **c,d** Simultaneously measured (**c**) in-situ RHEED and (**d**) ISHG intensities during growth of a  $(h\text{-YMnO}_3)_1/(h\text{-ErMnO}_3)_1$  superlattice where the oscillations in (**c**) and (**d**) are in phase as schematized in (**b**). **e,f** HAADF-STEM at room temperature after deposition confirms atomically sharp interfaces between the two constituents in the superlattice in (**c,d**). The heavier Er atoms appear brighter than the Y atoms. Note that the periodic displacement of the R-ions along the  $z$ -axis indicates the occurrence of ferroelectric polarization at room temperature in this particular superlattice. Its presence or absence is another aspect that can be growth-controlled by epitaxial constraints as detailed elsewhere<sup>18</sup>.

senses the symmetry of the bulk crystal lattice. We therefore find complementary information in combining the two in-situ methods. In particular, in the case of crystallographic defects or growth-mode variations, there can be a discrepancy between the most consolidated symmetry state (local minimum or maximum for ISHG) and the smoothest surface

(local maximum for RHEED intensity), as sketched in Fig. 4a. This can manifest as a phase shift between the RHEED and the ISHG oscillations (see Supplementary Figs. S1 and S2). Therefore, a surface-roughness-controlled heterostructure may not necessarily be the same as a symmetry-controlled heterostructure. On the other hand, by achieving a 2D layer-by-layer growth mode with a synchronization of both surface and symmetry variations, through a synchronization of the RHEED and ISHG oscillations, where each RHEED maximum corresponds to a local minimum or maximum for ISHG (Fig. 4b), we can combine the two techniques towards the design of symmetry-controlled interfaces with minimal interface roughness.

To demonstrate this, we grow a  $(\text{h-YMnO}_3)_1/(\text{h-ErMnO}_3)_1$  superlattice. The excellent lattice matching between  $\text{YMnO}_3$  and  $\text{ErMnO}_3$  increases our chances of maintaining a layer-by-layer growth mode with smooth interfaces during deposition. RHEED and ISHG data in Fig. 4c,d show that the respective signal oscillations are in phase. Each RHEED maximum coincides with a maximum or minimum of the ISHG signal. Hence, when the heterostructure acquires a state of complete centrosymmetry, it also exhibits the flattest surface. We verify the high precision of layering in this symmetry-controlled heterostructure at the atomic scale using high-angle annular dark-field scanning transmission electron microscopy (HAADF-STEM). Due to their large difference in atomic number, Y and Er can be clearly distinguished in the images (Fig. 4e,f). This reveals perfect alternation of Y and Er layers in the heterostructure. Thus, we not only verify the coveted two-dimensional growth mode but we also confirm that no intermixing at the atomic scale occurs.

## CONCLUSION

In conclusion, we have demonstrated the use of a sub-unit-cell growth mode in layered oxides for deterministic control of the resulting symmetry. Using the hexagonal manganites,  $\text{h-RMnO}_3$ , as model system, we show how deposition of only a half-unit-cell layer decides about the centrosymmetric or noncentrosymmetric nature of the epitaxially grown thin film. This control is enabled by the inherent noncentrosymmetry of the individual half-unit-cell layers, such that an odd number of these breaks inversion symmetry, while an even number preserves it. We have further shown that this symmetry alternation prevails in superlattices composed of different  $\text{h-RMnO}_3$  compounds and is independent of our choice of R-ions. We

emphasize that the emergence of symmetry-breaking functionalities at the sub-unit-cell level is not at all limited to the h-RMnO<sub>3</sub> system. In fact, we expect similar properties in any layered material composed of sub-unit-cell layers with reduced local symmetry. In expanding beyond the aspect of inversion symmetry, this sub-unit-cell control can be used to alternate the presence and absence of other parity-like properties like chirality, magnetic reciprocity etc. Thus, tracking and controlling thin-film oxide growth on the sub-unit-cell level has the potential to open up a new route for tailoring symmetry and coercing novel functionality in the ultrathin regime.

## METHODS

*Thin-film growth* The h-RMnO<sub>3</sub> films were grown by pulsed laser deposition using a KrF excimer laser at 248 nm. Stoichiometric ceramic targets were laser ablated with an energy fluence of 0.9 mJ cm<sup>-2</sup> at a substrate temperature of 800°C and in an oxygen partial pressure of 0.12 mbar. Before thin-film deposition, each substrate was annealed in air at 1250°C for 12 h.

*In-situ second harmonic generation* A pulsed Ti:Sapphire laser at 800 nm with a pulse duration of 45 fs and repetition rate of 1 kHz was converted using an optical parametric amplifier to the probe wavelength. The photon energy of the probe beam was set to 1.44 eV ( $\lambda = 860$  nm) with the ISHG intensity detected at 2.88 eV, close to resonances stemming from electronic Mn  $d-d$  transitions in the material<sup>19</sup>, thus enhancing the sensitivity to the local symmetry of the MnO<sub>5</sub> sublattices. The probe beam was incident on the sample with a pulse energy of 20  $\mu$ J on a spot size 250  $\mu$ m in diameter. The generated light intensity (ISHG) was subsequently detected using a monochromator and a photomultiplier system. Unless otherwise noted, the ISHG measurements were performed at  $\varphi = 45^\circ$ .

*Scanning transmission electron microscopy* Electron transparent cross-sectioned samples for transmission electron microscopy were prepared by means of a FEI Helios NanoLab 600i focused ion beam (FIB) operated at accelerating voltages of 30 and 5 kV. High-angle annular dark-field scanning transmission electron microscopy (HAADF-STEM) was carried out on a FEI Titan Themis with a probe CEOS DCOR spherical aberration corrector operated at 300 kV. A probe semiconvergence angle of 25.3 mrad was used in combination with an annular semidetector range of the annular dark-field detector set to collect electrons

206 scattered between 90 and 370 mrad.

## 207 ACKNOWLEDGMENTS

208 The authors thank Ch. Tzschaschel for fruitful discussions. J.N., M.T. and M.F. ac-  
209 knowledge financial support by the EU European Research Council under Advanced Grant  
210 Program No. 694955-INSEETO. M.T. acknowledges financial support by the Swiss National  
211 Science Foundation under Project No. 200021\_188414. M.D.R. and M.C. acknowledge sup-  
212 port by the Swiss National Science Foundation under Project No. 200021\_175926.

- 
- 213 [1] M. Livio, Physics: Why symmetry matters, *Nature* **490**, 472 (2012).  
214 [2] N. P. Armitage, E. J. Mele, and A. Vishwanath, Weyl and Dirac semimetals in three-  
215 dimensional solids, *Reviews of Modern Physics* **90**, 015001 (2018).  
216 [3] S. Trolier-McKinstry and P. Muralt, Thin Film Piezoelectrics for MEMS, *Journal of Electro-*  
217 *ceramics* **12**, 7 (2004).  
218 [4] V. M. Fridkin, Bulk photovoltaic effect in noncentrosymmetric crystals, *Crystallography Re-*  
219 *ports* **46**, 654 (2001).  
220 [5] F. Hellman et al., Interface-induced phenomena in magnetism, *Reviews of Modern Physics*  
221 **89**, 025006 (2017).  
222 [6] H. Y. Hwang, Y. Iwasa, M. Kawasaki, B. Keimer, N. Nagaosa, and Y. Tokura, Emergent  
223 phenomena at oxide interfaces, *Nature Materials* **11**, 103 (2012).  
224 [7] A. Ohtomo and H. Hwang, A high-mobility electron gas at the  $\text{LaAlO}_3/\text{SrTiO}_3$  heterointerface,  
225 *Nature* **427**, 423 (2004).  
226 [8] N. Sai, B. Meyer, and D. Vanderbilt, Compositional inversion symmetry breaking in ferroelec-  
227 tric perovskites, *Physical Review Letters* **84**, 5636 (2000).  
228 [9] H. N. Lee, H. M. Christen, M. F. Chisholm, C. M. Rouleau, and D. H. Lowndes, Strong  
229 polarization enhancement in asymmetric three-component ferroelectric superlattices, *Nature*  
230 **433**, 395 (2005).  
231 [10] C. Becher, M. Trassin, M. Lilienblum, C. T. Nelson, S. J. Suresha, D. Yi, P. Yu, R. Ramesh,  
232 M. Fiebig, and D. Meier, Functional ferroic heterostructures with tunable integral symmetry,

- Nature Communications **5**, 4295 (2014).
- [11] K. F. Mak, C. Lee, J. Hone, J. Shan, and T. F. Heinz, Atomically thin MoS<sub>2</sub>: A new direct-gap semiconductor, Physical Review Letters **105**, 136805 (2010).
- [12] W. Yao, D. Xiao, and Q. Niu, Valley-dependent optoelectronics from inversion symmetry breaking, Physical Review B **77**, 235406 (2008).
- [13] N. Kumar, S. Najmaei, Q. Cui, F. Ceballos, P. M. Ajayan, J. Lou, and H. Zhao, Second harmonic microscopy of monolayer MoS<sub>2</sub>, Physical Review B **87**, 161403 (2013).
- [14] W.-T. Hsu, Z.-A. Zhao, L.-J. Li, C.-H. Chen, M.-H. Chiu, P.-S. Chang, Y.-C. Chou, and W.-H. Chang, Second harmonic generation from artificially stacked transition metal dichalcogenide twisted bilayers, ACS Nano **8**, 2951 (2014).
- [15] X. Yin, Z. Ye, D. A. Chenet, Y. Ye, K. O’Brien, J. C. Hone, and X. Zhang, Edge nonlinear optics on a MoS<sub>2</sub> atomic monolayer, Science **344**, 488 (2014).
- [16] G. De Luca, N. Strkalj, S. Manz, C. Bouillet, M. Fiebig, and M. Trassin, Nanoscale design of polarization in ultrathin ferroelectric heterostructures, Nature Communications **8**, 1419 (2017).
- [17] J. Nordlander, G. De Luca, N. Strkalj, M. Fiebig, and M. Trassin, Probing Ferroic States in Oxide Thin Films Using Optical Second Harmonic Generation, Applied Sciences **8**, 570 (2018).
- [18] J. Nordlander, M. Campanini, M. D. Rossell, R. P. Erni, Q. N. Meier, A. Cano, N. A. Spaldin, M. Fiebig, and M. Trassin, The ultrathin limit of improper ferroelectricity, Nature Communications **10**, 5591 (2019).
- [19] C. Degenhardt, M. Fiebig, D. Fröhlich, T. Lottermoser, and R. V. Pisarev, Nonlinear optical spectroscopy of electronic transitions in hexagonal manganites, Applied Physics B **73**, 139 (2001).
- [20] M. Fiebig, V. V. Pavlov, and R. V. Pisarev, Second-harmonic generation as a tool for studying electronic and magnetic structures of crystals: review, Journal of the Optical Society of America B **22**, 96 (2005).
- [21] S. A. Denev, T. T. A. Lummen, E. Barnes, A. Kumar, and V. Gopalan, Probing Ferroelectrics Using Optical Second Harmonic Generation, Journal of the American Ceramic Society **94**, 2699 (2011).

- 263 [22] V. Jähnke, U. Conrad, J. Gütde, and E. Matthias, SHG investigations of the magnetization  
264 of thin Ni and Co films on Cu(001), *Applied Physics B: Lasers and Optics* **68**, 485 (1999).
- 265 [23] R. R. Birss, *Symmetry and magnetism*, Vol. 863 (North-Holland Pub. Co., 1964).
- 266 [24] C. J. Fennie and K. M. Rabe, Ferroelectric transition in YMnO<sub>3</sub> from first principles, *Physical*  
267 *Review B* **72**, 100103 (2005).